Lamb wave mode conversion and multiple-reflection mechanisms for simply and reliably evaluating delamination in composite laminates

Ryuzono, Kazuki
Department of Aeronautics and Astronautics, Kyushu University

Yashiro, Shigeki
Department of Aeronautics and Astronautics, Kyushu University

Onodera, Sota
Department of Aeronautics and Astronautics, Kyushu University

Toyama, Nobuyuki
National Metrology Institute of Japan, National Institute of Advanced Industrial Science and Technology (AIST)

https://hdl.handle.net/2324/6781063

KYUSHU UNIVERSITY

Lamb wave mode conversion and multiple-reflection mechanisms for simply and reliably evaluating delamination in composite laminates

Kazuki Ryuzono[a,*], Shigeki Yashiro[a], Sota Onodera[a], Nobuyuki Toyama[b]

aDepartment of Aeronautics and Astronautics, Kyushu University, 744 Motooka, Nishi-ku, Fukuoka 819-0395, Japan; bNational Metrology Institute of Japan, National Institute of Advanced Industrial Science and Technology (AIST), 1-1-1 Umezono, Tsukuba, Ibaraki 305-8568, Japan

*Corresponding author: Ryuzono@aero.kyushu-u.ac.jp (K. Ryuzono)

Lamb wave mode conversion and multiple-reflection mechanisms for simply and reliably evaluating delamination in composite laminates

Lamb wave propagation must be understood comprehensively for simply evaluating delamination during ultrasonic testing. However, the difference between wave propagation, visualized using laser Doppler vibrometer and pulsed-laser scanners, has not been sufficiently investigated, and knowledge of optimal conditions for evaluating delamination is limited. Thus, in this study, the mode conversion and multiple reflections of Lamb waves propagating in a delaminated cross-ply laminate were visualized using different laser scanners, delamination depths, and wave incident angles. Delamination was characterized using maximum-amplitude map postprocessing under specific conditions. Further numerical analysis revealed that owing to multiple reflections of the antisymmetric mode in incident and mode-converted waves, standing waves were generated in the delaminated sublaminate. Dispersion curve and flexural stiffness calculations confirmed the conditions required for high-amplitude standing waves, thereby providing guidelines for simply and reliably evaluating delamination during inspections.

Keywords: nondestructive testing; polymer-matrix composites; delamination; laser ultrasonic imaging; Lamb wave propagation; standing waves

1. Introduction

Carbon-fiber-reinforced plastic (CFRP) with high specific stiffness and strength is increasingly being used in various structures such as transportation equipment and social infrastructure. During long-term operation, composite engineering structures are damaged in a complex manner over their lifetime [1]. Among the various types of damage, out-of-plane impact-induced delamination considerably reduces the residual compressive strength of composite structures. Because compressive strength reduction depends on the delaminated area size [2,3], the latter must be quantitatively nondestructively evaluated to enhance structural reliability.

Ultrasonic testing has been widely used for inspecting composite structures

because ultrasonic waves are highly sensitive to internal defects such as delamination. However, conventional ultrasonic testing using point measurements can overlook or misidentify defects because interpreting ultrasonic signals is complicated [4–6]. Moreover, ultrasonic waves propagate as guided Lamb waves [7] with dispersive nature in thin plate-like structures such as aircraft skins and automobile bodies. Comprehensively understanding Lamb waves, including multimode waves generated by interactions with unknown defects and medium boundaries, is very challenging. Therefore, most studies have developed measurement systems combined with signal-processing and feature-extraction methods and have investigated Lamb wave propagation mechanisms for inspecting defects [8,9].

Defect detection is facilitated using laser scanning systems to visualize anomalous ultrasonic waves. For instance, laser Doppler vibrometer (LDV) [10,11] and pulsed-laser systems [12] have previously been developed for ultrasonic reception and excitation, respectively, to detect delamination and adhesive disbond in composite structures [13–15]. Despite the apparent success of visualization systems, however, quantitatively evaluating defect locations, sizes, and shapes remains challenging, and most studies have incorporated signal-processing and feature-extraction methods [16]. Reflected, standing, and mode-converted waves generated by defects have previously been separated using frequency-domain analysis [17,18]. Moreover, specific ultrasonic wave features such as amplitudes and wavenumbers have also been extracted [13,19–21], and deep learning or topology optimization techniques have been used to visualize defects [22–24].

Although previous studies [13,16–24] have focused on highly challenging postprocessing techniques to characterize delamination by visualizing any propagating wave, simple complex-postprocessing-free evaluation techniques are promising

candidates for application to actual inspections. Additionally, because changes in Lamb wave propagation characteristics have not yet been considered under different conditions in delaminated regions, wave propagation characteristics and mechanisms must be comprehensively investigated to evaluate delamination more simply and reliably. Previously, standing Lamb waves have been visualized in delaminated areas [13,19,21]. These Lamb waves were generated by multiple reflections of the Lamb wave antisymmetric mode in delaminated sublaminates [25]. Additionally, converting the symmetric mode to the antisymmetric one generated standing waves in delaminated areas [26]. Moreover, standing-wave amplitudes varied considerably, depending on the delamination depth [26–28]. Although the relationship between the standing-wave amplitude and the sublaminate resonance frequency has been investigated previously [29], there have been few studies on the mechanisms through which standing-wave amplitudes vary depending on the delamination geometry and wave propagation conditions. Furthermore, although standing waves have been experimentally monitored using only LDV scanning [13,19,21,26–28,30], to the best of our knowledge, these results have not been compared with the results obtained using more-practical pulsed-laser scanning. Therefore, Lamb wave propagation characteristics and mechanisms must be further investigated in delaminated laminates to provide fundamental knowledge for developing signal-processing and feature-extraction techniques.

Therefore, we experimentally visualized Lamb waves propagating in a delaminated cross-ply laminate to investigate propagation characteristics and mechanisms based on mode conversion and multiple reflections. Initially, different scanning systems were used to visualize Lamb waves propagating parallel and perpendicular to the surface fiber orientation of a film-inserted cross-ply laminate to elucidate wave propagation characteristic changes under different conditions.

Subsequently, the experimentally visualized wave propagation was reproduced using dynamic finite element analysis, and the wave propagation mechanisms were elucidated based on sublaminate dispersion curves and flexural stiffnesses. The conditions under which high-amplitude standing Lamb waves were generated in the delaminated area were specified for simply and quantitatively evaluating delamination. Finally, simple postprocessing was used to experimentally evaluate barely visible impact damage (BVID) in a cross-ply laminate to verify the specified conditions.

2. Experimental

2.1. Specimens

Two cross-ply laminates of dimensions 160 mm × 160 mm × 2 mm (Specimens I and II) were prepared using CFRP (T700SC/2592, Toray), and the stacking sequence was $[0_4/90_4]_s$. Specimen I was artificially centrally delaminated using double-layered polyimide films of dimensions 10 mm × 10 mm × 0.03 mm (Kapton®, DuPont) at a 0/90° interface. Specimen II was impacted at low velocity using a vertical drop-weight impact system (CEAST 9310, Instron) to induce BVID, and the impact generated 5 J. The specimens were preliminarily inspected using a water-immersion ultrasonic C-scan system (G-SCAN 6AX500, GNES) operating at a constant scan spacing (0.25 mm) and a 5-MHz-resonance focused ultrasonic transducer. The C-scan images clearly exhibited delamination (Fig. 1). The artificial delamination area in Specimen I was slightly smaller than 10 mm × 10 mm because a trace of resin had flowed between both films during molding. The BVID in Specimen II exhibited peanut-shaped delamination of dimensions 25.5 mm × 9.8 mm along the major and minor axes, respectively, at the 0/90° interface opposite the impact surface. Usually, cross-ply laminates impacted at low velocity delaminate at the interface opposite the impact surface [31]. The impact

surface of Specimen II exhibited only a small dent. These defects were the identification targets for this study.

2.2. Laser scanning systems

As shown in Fig. 2, ultrasonic waves were visualized using either a fixed-point transducer and scanning laser or *vice versa* (hereafter called 'F/S system' or 'S/F system') for ultrasonic excitation and reception, respectively. In the F/S system (Fig. 2a), five-period 200-kHz sinusoidal waves—exhibiting a frequency of 200 kHz multiplied by a Hanning window—were generated using a multifunction generator (WF1974, NF Corporation), amplified using a high-speed bipolar amplifier (BA4825, NF Corporation), and excited using a fixed 200-kHz-resonance piezoelectric (PZT) transducer (PW B0.2K20N, Japan Probe) in contact with the specimen. The inspected area was scanned using LDV (PSV-500-M, Polytec), and the out-of-plane displacement at each illuminated point was measured based on the Doppler effect. The measured signals were bandpass-filtered from 50 to 400 kHz and were stored on a computer using a data acquisition board (PCI-6110, National Instruments). The excitation frequency, waveform, and cut-off frequencies were determined so that ultrasonic waves only propagated as the S0 and A0 fundamental Lamb modes to avoid the dispersive nature of Lamb waves, as described in following Section 3.1. The visualized ultrasonic wave propagation originating from the fixed transducer was obtained by plotting the amplitude of each waveform on a contour map in the measurement time order.

The S/F system (Fig. 2b) used a Q-switched pulsed laser (Onda 1064 nm, Bright Solutions) with a wavelength of 1064 nm, pulse width of 2 ns and maximum pulse energy of 1.5 mJ. The laser beam was focused through an electrically focused tunable lens (EL-10-30-Ci, Optotune) and scanned using a computer-controlled galvanometer mirror (VM500+, Novanta). The thermoelastic ultrasonic waves generated at the

illuminated points were received by a fixed 200-kHz-resonance PZT transducer (M204A R-CAST AE sensor, Fuji Ceramics) in contact with the specimen. The reception frequency was determined for the same reason as the excitation frequency of the F/S system. The signals were amplified using a preamplifier (A1201, Fuji Ceramics), high-pass filtered at 20 kHz using a variable-frequency filter (3628 Dual Channel Programmable Filter, NF Corporation), and stored using a high-speed digitizer (NI PXI-5124, National Instruments) on a computer. Based on the reciprocity assumption of wave propagation [12,14], the visualized wave propagation originating from the fixed transducer was obtained in the same manner as that visualized using the F/S system.

2.3. Measurement conditions

As shown in Fig. 3a, ultrasonic waves propagating parallel (e.g., incident angle $\theta = 0°$) and perpendicular (e.g., $\theta = 90°$) to the surface fiber orientation were visualized using both systems. Because the waves were measured on the front (impact) and back surfaces as shown in Fig. 3b, eight measurement condition combinations comprising laser scanning systems, surfaces, and wave incidence angles were possible for a single specimen. A 50 mm × 50 mm area centered on the delamination was scanned, and the PZT transducer was fixed 40 mm from the delamination (Fig. 3a). The F/S and S/F system scan spacings were 0.5 and 0.25 mm (101 × 101 and 198 × 198 points), respectively, and the acquisition time was 100 μs. For the F/S system, the specimen surface was painted white, and 10 signals were measured and averaged at each scanned point, to improve the signal-to-noise (S/N) ratio.

3. Results and discussion

3.1. Lamb wave visualization in film-inserted specimen

Potential Lamb wave modes were preliminarily investigated. When Lamb waves propagated parallel to (e.g., at $\theta = 0°$) the surface fiber orientation on $[0_4/90_4]_S$, they passed through sublaminates $[0_4/90_8]_T$ and $[0_4]_T$ in the delaminated region. Similarly, at $\theta = 90°$, the entire laminate and sublaminates comprised $[90_4/0_4]_S$, $[90_4/0_8]_T$, and $[90_4]_T$. Figure 4 shows the dispersion curves of the Lamb waves propagating in these possible stacking sequences, as calculated using the Dispersion Calculator [32] and the material properties listed in Table 1. At a 200-kHz transducer resonance, the ultrasonic waves only propagated as the S0 and A0 fundamental modes in all the stacking sequences. Although the Lamb modes propagating in the asymmetric sublaminates are usually neither symmetric nor antisymmetric, the longer-wavelength, higher-velocity mode is referred to as the 'S0 mode,' whereas the other mode is referred to as the 'A0 mode' for convenience.

Figure 5 shows the snapshots of the visualized Lamb waves propagating on the back surface of Specimen I. The black dotted line outlines the delamination region in the C-scan image (Fig. 1a). Although the incident waves exhibited both the long-wavelength, high-velocity S0 and short-wavelength, low-velocity A0 modes, noise remained in the snapshots captured using the F/S system (Figs. 5a, b, e, f), and the A0 mode rung owing to contact transducer resonance in the S/F system (Fig. 5h). The fast S0 and slow A0 modes reached the delaminated region at different time. When only the incident S0 mode reached the delaminated region (Figs. 5a–d), the higher-amplitude wave than the incident S0 mode was generated in the delaminated region. Its wavelengths were about 5 and 3 mm in parallel and perpendicular directions to the surface fiber orientation, respectively. These wavelengths agreed with those of the A0 mode calculated from the dispersion curves (Fig. 4), indicating that the incident S0

mode was converted to the A0 one in the delaminated region. Standing waves of the A0 mode converted from the incident S0 one were then visualized in the delaminated region regardless of the incident angle. Moreover, when the incident A0 mode reached the delaminated region (Figs. 5e–h), the incident A0 mode was repeatedly reflected, and the standing waves by these multiple reflections remained in the delaminated region even after the incident A0 mode had passed through it. All the measurements on the back surface exhibited these phenomena.

Figure 6 shows the maximum-amplitude maps of the visualized wave propagation shown in Fig. 5, i.e., the distribution obtained by plotting the maximum absolute value of the actual out-of-plane displacement and voltage at each point scanned using the F/S and S/F systems, respectively. In the maximum-amplitude maps generated for the S0 (and mode-converted) waves (Figs. 6a–d), the high-amplitude region in the maps captured using the S/F system (Figs. 6c, d) coincided with the delamination outline. In the maximum-amplitude maps generated for the entire signal (Figs. 6e–h), the high-amplitude region in the maps generated for $\theta = 90°$ using the F/S system (Fig. 6f) and for $\theta = 0°$ using the S/F system (Fig. 6g) agreed well with the delamination outline.

Figure 7 shows the snapshots and maps generated using the S/F system to scan the front surface. The S0 mode was clearly converted to the A0 one at $\theta = 0°$ (Fig. 7a), and the high-amplitude region in the maximum-amplitude map (Fig. 7b) coincided with the delamination outline. However, insufficient multiple reflections of the incident A0 mode were generated to use the maximum-amplitude map to evaluate the delaminated area (Figs. 7e, f). The remaining maps generated for the front surface (Figs. 7c, d, g, h), including those generated using the F/S system, did not show sufficient clear mode conversions and multiple reflections to image delamination.

These results suggest that the standing waves generated by multiple reflections of the incident A0 mode were most observable using the F/S system at $\theta = 90°$ on the back surface. Moreover, the standing waves generated by multiple reflections of the S0/A0-mode-converted wave were easily visualized using the S/F system at $\theta = 0$ and 90° on the back surface and at $\theta = 0°$ on the front surface.

3.2. Mechanism investigation

Dynamic finite element analysis was used to investigate the mechanisms of Lamb wave propagation in the delaminated sublaminates. The numerical model of dimensions 160 mm × 160 mm × 2 mm (Fig. 8) was discretized using eight-node hexahedral solid elements of dimensions 0.5 mm × 0.5 mm × 0.125 mm. The stacking sequence was $[0_4/90_4]_s$, and the lower 0/90° interface was bonded using uniparameter cohesive elements [35] to simulate delamination. The internal residual strength parameter (s) was set to 0 (i.e., delaminated) and 0.9 (i.e., intact) in the central 10 mm × 10 mm region and other regions, respectively, throughout the analysis. Because the wave propagation negligibly changed even when the delaminated interface contact was considered, contact was neglected to improve the wave visibility. The numbers of solid and cohesive elements and nodes were 1638400, 102400, and 1854738, respectively. The CFRP material properties are listed in Table 1. A five-period 200-kHz sinusoidal-wave load multiplied by a Hanning window was applied in the through-thickness direction at a single node of the fixed transducer position. All the remaining boundaries were free-ended. The timestep was 0.01 μs, which satisfied the Courant condition in dynamic finite element analysis. This analysis corresponds to the experiments conducted using the F/S system.

Figure 9 shows the numerical results of the Lamb wave propagation and

maximum-amplitude map generated by plotting the out-of-plane displacement at each node. The S0 mode was almost undetectable in incident waves because of the small amplitude. At $\theta = 90°$ on the back surface, standing waves were generated after the S0 mode was converted to the A0 one (Fig. 9a), and multiple reflections of the incident A0 mode were most clearly visualized in the delaminated area (Fig. 9e). The delamination size was characterized by the high-amplitude region in the maximum-amplitude map (Figs. 9b, f). At $\theta = 0°$ on the front surface, the S0 mode was converted to the A0 one (Figs. 9c, d), whereas multiple reflections of the incident A0 mode were unobservable (Figs. 9g, h). Although multiple reflections of the incident and mode-converted A0-mode were visible at $\theta = 0°$ on the back surface, the reflections were less clear than those visualized at $\theta = 90°$ on the back surface. At $\theta = 90°$ on the front surface, multiple reflections of the incident A0 mode were barely observable and among all the measurement conditions, the S0 mode converted the least to the A0 one. The numerical results (Figs. 9a, b, e, f) obtained at $\theta = 90°$ on the back surface were similar to the experimental observations obtained using the F/S system (Figs. 5b, f and 6b, f), and the remaining numerical results were consistent with the corresponding experimental ones (Figs. 5–7).

The conditions and mechanisms required for generating high-amplitude standing waves in the delaminated region are now discussed based on the dispersion curves (Fig. 4) and flexural stiffnesses (Table 2) of the possible sublaminate stacking sequences. Figure 10 shows the snapshots of waves propagating in the cross-section indicated by the black dashed lines shown in Figs. 9e and g when the incident A0 mode reached the delaminated region. At incident angle $\theta = 90°$, Lamb waves propagated through sublaminates $[90_4/0_8]_T$ and $[90_4]_T$ in the delaminated area, as described in Section 3.1. When the A0 mode was incident to the delamination, the difference between the A0-

mode velocities propagating through sublaminates $[90_4/0_8]_T$ and $[90_4]_T$ (Fig. 4d)

generated different A0-mode phases (Fig. 10a). Reflected waves were required for

phase-aligned A0 mode waves to pass through the delamination exit edge (Fig. 10b),

and the reflected-wave amplitude was higher in sublaminate $[90_4]_T$ than in $[90_4/0_8]_T$

because $[90_4]_T$ was relatively thin and exhibited much lower flexural stiffness than

$[90_4/0_8]_T$. The reflected A0 mode reached the other delamination edge and was

repeatedly reflected. These multiple reflections generated standing waves that remained

in the delaminated region (Fig. 10c). At $\theta = 0°$, although the differences between the

A0-mode velocities (Fig. 4c) and phases (Fig. 10d) were minimal in sublaminates

$[0_4/90_8]_T$ and $[0_4]_T$, the A0 mode was reflected at the delamination edge (Fig. 10e), and

higher-amplitude standing waves were generated in sublaminate $[0_4]_T$, which exhibited

lower flexural stiffness than $[0_4/90_8]_T$ (Fig. 10f). However, in sublaminate $[0_4]_T$, the

standing-wave amplitude was comparable to the incident A0 one and was insufficient to

use maximum-amplitude map to characterize the delaminated region. Conversely, the

high-amplitude standing waves which could be utilized to evaluate delamination were

generated in sublaminate $[90_4]_T$ because the flexural stiffness was considerably different

in the sublaminates above and below the delaminated region.

High-amplitude standing waves were also generated by multiple reflections of

the S0/A0-mode-converted wave in the delaminated region. Figure 11 shows the

snapshots of waves propagating in the cross-section indicated by the black dashed lines

shown in Figs. 9a and c when only the incident S0 mode reached the delaminated

region. The S0-mode displacement field, which was symmetrical to the entire laminate

neutral plane, exhibited antisymmetric to the thinner sublaminate neutral one (Figs. 11a,

b). The incident S0 mode was converted to the A0 one when the S0 mode reached both

the delaminated region entrance and exit edges (Fig. 11b). After the S0 mode was

converted to the A0 one, multiple reflections of the mode-converted A0-mode were generated, thereby generating standing waves (Fig. 11c). Furthermore, at $\theta = 0°$, the S0 mode was converted to the A0 one even in the thicker sublaminate. The out-of-plane displacement of the high-amplitude S0 mode near the surface ply involved the entire sublaminate $[0_4/90_8]_T$, thereby converting the S0 mode to the A0 one (Fig. 11e). Conversely, at $\theta = 90°$, the S0 mode was not clearly converted to the A0 one in the thicker sublaminate (Figs. 11b, c). These results indicate that in the thicker sublaminates, an out-of-plane displacement exhibiting the same sign in the entire sublaminate was easily generated when the flexural stiffnesses of the plies near the delaminated region were lower than those of the plies near the surface considerably deformed by the incident S0 mode, which converted the S0 mode to the A0 one. Therefore, to utilize the standing waves generated by the mode-converted A0-mode on the front surface, Lamb waves propagating parallel to the surface fiber orientation should be captured.

These results suggest that in the delaminated area, standing Lamb waves were generated on the back surface at $\theta = 90°$ or at $\theta = 0$ and $90°$ owing to multiple reflections of the incident A0 mode or of the S0/A0-mode-converted wave, respectively. The latter is also valid at $\theta = 0°$ on the front surface. However, as discussed in Section 3.1, the maximum-amplitude map generated using the F/S system did not exhibit any evidence of S0/A0-mode conversion (Figs. 6a, b) because when the S0 mode was converted to the A0 one, the latter exhibited a lower amplitude than the noise owing to the low LDV S/N ratio. Conversely, in the maximum-amplitude map generated using the S/F system, the A0 mode thermoelastically generated and propagating at $\theta = 0°$ exhibited a low amplitude owing to the low coefficient of thermal expansion in the fiber direction, and the map clearly exhibited S0/A0-mode conversion (Figs. 6c, g, and 7b).

Furthermore, at $\theta = 90°$, multiple reflections of the incident A0 mode were barely observable when the S/F system was used to generate the map (Fig. 6h), because the incident A0 mode rung owing to contact transducer resonance and exhibited a high amplitude owing to the high coefficient of thermal expansion in the surface-ply transverse direction. In a previous study [36], however, the A0 mode ringing disappeared using a fully noncontact measurement system. Therefore, when the fully noncontact system is used, the experimental and numerical results will agree well.

3.3. BVID inspection

The specified conditions under which the standing waves could characterize delamination were verified by evaluating actual delamination in Specimen II. Figure 12 shows the wave propagation visualized on and the maximum-amplitude map generated for the back surface. Standing waves originating from multiple reflections of the incident A0 mode (Figs. 12e, g) and S0/A0-mode-converted wave (Figs. 12a, c) were generated in the delaminated area. Under all the specified conditions, the high-amplitude region in the maximum-amplitude maps (Figs. 12b, d, f, h) was consistent with the BVID outline in the C-scan image (Fig. 1b). Even when the front surface far from the delaminated interface was inspected (Fig. 13), the standing waves generated by multiple reflections of the S0/A0-mode-converted wave in the delaminated area were extracted using the S/F system to visualize the waves propagating at $\theta = 0°$. However, as shown in Figs. 12d and 13b, a part of the delaminated region far from the fixed transducer was not clearly characterized by standing waves of the S0/A0 mode-converted wave propagating at $\theta = 0°$ owing to the peanut-shaped delamination aligned in the $\theta = 0°$ direction. Therefore, sufficient spacing should be provided between the target defect and fixed transducer to separate the fast S0 mode from the slow A0 one.

These results indicate that when either surface is inspected, delamination should be inspected from the surface opposite the impact one and that if the back surface cannot be accessed, delamination should be evaluated based on the visualized Lamb waves propagating parallel to the surface fiber orientation.

4. Conclusions

In delaminated regions, Lamb wave mode conversion and multiple reflections were experimentally visualized using different laser scanning systems, delamination depths, and wave incident angles, and the mode conversion and reflection mechanisms were numerically investigated. This study concluded that the mode conversion and multiple reflections were generated at the delamination edges based on the following mechanisms. Multiple reflections of the incident A0 mode were generated owing to the difference between the A0-mode phases in sublaminates stacked in different sequences above and below the delamination. The multiple reflections exhibited higher amplitudes in the lower-flexural-stiffness sublaminate, particularly when the sublaminates exhibited considerably different flexural stiffnesses above and below the delamination. Moreover, the S0 mode was converted to the A0 one in the delaminated region because the deformation field in the S0 mode symmetric to the entire laminate neutral plane was antisymmetric to the thinner sublaminate neutral one. The S0 mode was also converted to the A0 one in the thicker sublaminates because the out-of-plane displacement exhibiting the same sign in the entire sublaminate was easily generated when the flexural stiffnesses of the plies near the delaminated region were lower than those of the plies near the surface. Multiple reflections of the S0/A0-mode-converted wave exhibited higher amplitudes than the incident S0 mode. Owing to these multiple reflections, high-amplitude standing waves were utilized to evaluate delamination simply and quantitatively. According to the proposed wave propagation mechanisms, although

delamination should be ultrasonically tested from the surface opposite the impact one (i.e., thinner sublaminate), Lamb waves propagating parallel to the surface fiber orientation are useful if the target can only be accessed from the impact surface (i.e., thicker sublaminate).

With a few exceptions, the BVID in a cross-ply laminate was evaluated and identified under all the specified conditions by extracting only the maximum-amplitude from the ultrasonic signals at each scanned point. In the F/S system, standing waves generated by the S0/A0-mode-converted waves exhibited lower amplitudes than those of the LDV noise. In the S/F system, on the other hand, multiple reflections of the incident A0 mode were invisible because of contact transducer ringing in the incident high-amplitude A0 mode because the coefficient of thermal expansion was high in the surface-ply transverse direction. The experimental and numerical investigations of the Lamb wave propagation characteristics and mechanisms provide fundamental insight for developing Lamb-wave-based damage evaluation techniques.

References

[1]   Talreja R, Singh CV. Damage and failure of composite materials. Cambridge (UK): Cambridge University Press; 2012.

[2]   Ghelli D, Minak G. Low velocity impact and compression after impact tests on thin carbon/epoxy laminates. Compos Part B. 2011;42(7):2067–2079.

[3]   Sun XC, Hallett SR. Failure mechanisms and damage evolution of laminated composites under compression after impact (CAI): Experimental and numerical study. Compos Part A. 2018;104:41–59.

[4]   Krautkrämer J, Krautkrämer K. Ultrasonic Testing of Materials. 4th ed. Berlin: Springer; 1990.

[5]   Adams RD, Cawley P. A review of defect types and nondestructive testing

techniques for composites and bonded joints. NDT Int. 1988;21(4):208–222.

[6]   Wang B, Zhong S, Lee T-L, Fancey KS, Mi J. Non-destructive testing and evaluation of composite materials/structures: A state-of-the-art review. Adv. Mech. Eng. 2020;12(4):1–28.

[7]   Rose JL. Ultrasonic waves in solid media. Cambridge (UK): Cambridge University Press; 1999.

[8]   Su Z, Ye L, Lu Y. Guided Lamb waves for identification of damage in composite structures: A review. J Sound Vib. 2006;295(3–5):753–780.

[9]   Mitra M, Gopalakrishnan S. Guided wave based structural health monitoring: A review. Smart Mater Struct. 2016;25:053001.

[10]   Mallet L, Lee BC, Staszewski WJ, Scarpa F. Structural health monitoring using scanning laser vibrometry: II. Lamb waves for damage detection. Smart Mater Struct. 2004;13:261.

[11]   Ruzzene M, Jeong SM, Michaels TE, Michaels JE, Mi B. Simulation and measurement of ultrasonic waves in elastic plates using laser vibrometry. AIP Conf Proc. 2005;760(1):172.

[12]   Takatsubo J, Wang B, Tsuda H, Toyama N. Generation laser scanning method for the visualization of ultrasounds propagating on a 3-D object with an arbitrary shape. J Solid Mech Mater Eng. 2007;1(12):1405–1411.

[13]   Sohn H, Dutta D, Yang JY, DeSimio M, Olson S, Swenson E. Automated detection of delamination and disbond from wavefield images obtained using a scanning laser vibrometer. Smart Mater Struct. 2011;20:045017.

[14]   Yashiro S, Takatsubo J, Toyama N. An NDT technique for composite structures using visualized Lamb-wave propagation. Compos Sci Technol. 2007;67(15–16):3202–3208.

[15]   Toyama N, Yamamoto T, Urabe K, Tsuda H. Ultrasonic inspection of adhesively bonded CFRP/aluminum joints using pulsed laser scanning. Adv Compos Mater. 2019;28(1):27–35.

[16]   Ostachowicz W, Radzieński M, Kudela P. 50th anniversary article: Comparison studies of full wavefield signal processing for crack detection. Strain. 2014;50(4):275–291.

[17]   Michaels TE, Michaels JE, Ruzzene M. Frequency-wavenumber domain analysis of guided wavefields. Ultrasonics. 2011;51(4):452–466.

[18]   Lee JR, Chia CC, Shin HJ, Park CY, Yoon DJ. Laser ultrasonic propagation imaging method in the frequency domain based on wavelet transformation. Opt Lasers Eng. 2011;49(1):167–175.

[19]   Park B, An YK, Sohn H. Visualization of hidden delamination and debonding in composites through noncontact laser ultrasonic scanning. Compos Sci Technol. 2014;100:10–18.

[20]   Rogge MD, Leckey CAC. Characterization of impact damage in composite laminates using guided wavefield imaging and local wavenumber domain analysis. Ultrasonics. 2013;53(7):1217–1226.

[21]   Kudela P, Wandowski T, Malinowski P, Ostachowicz W. Application of scanning laser Doppler vibrometry for delamination detection in composite structures. Opt Lasers Eng. 2017;99:46–57.

[22]   Ijjeh AA, Ullah S, Kudela P. Full wavefield processing by using FCN for delamination detection. Mech Sys Signal Process. 2021;153:107537.

[23]   Ryuzono K, Yashiro S, Nagai H, Toyama N. Topology optimization-based damage identification using visualized ultrasonic wave propagation. Materials. 2020;13(1):33.

[24] Ryuzono K, Yashiro S, Onodera S, Toyama N. Performance evaluation of crack identification using density-based topology optimization for experimentally visualized ultrasonic wave propagation. Mech Mater. 2022;172:104406.

[25] Hayashi T, Kawashima K. Multiple reflections of Lamb waves at a delamination. Ultrasonics. 2002;40(1–8):193–197.

[26] Wandowski T, Kudela P, Ostachowicz WM. Numerical analysis of elastic wave mode conversion on discontinuities. Compos Struct. 2019;215:317–330.

[27] Migot A, Mei H, Giurgiutiu V. Numerical and experimental investigation of delaminations in a unidirectional composite plate using NDT and SHM techniques. J Intel Mater Sys Struct. 2021;32(16):1781–1799.

[28] Hervin F, Maio L, Fromme P. Guided wave scattering at a delamination in a quasi-isotropic composite laminate: Experiment and simulation. Compos Struct. 2021;275:114406.

[29] Munian RK, Mahapatra DR, Gopalakrishnan S. Lamb wave interaction with composite delamination. Compos Struct. 2018;206:484–498.

[30] Pieczonka Ł, Ambroziński Ł, Staszewski WJ, Barnoncel D, Pérès P. Damage detection in composite panels based on mode-converted Lamb waves sensed using 3D laser scanning vibrometer. Opt Lasers Eng. 2017;99:80–87.

[31] Nishikawa M, Okabe T, Takeda N. Numerical simulation of interlaminar damage propagation in CFRP cross-ply laminates under transverse loading. Int J Solids Struct. 2007;44(10):3101–3113.

[32] Huber AMA, Sause MGR. Classification of solutions for guided waves in anisotropic composites with large numbers of layers. J Acoust Soc Am. 2018;144(6):3236–3251.

[33] Yashiro S, Agata T, Yoshimura Y. New test method for mode II interlaminar

fracture toughness of composite laminates: doubly end-notched tension method. J
Jpn Soc Compos Mater. 2018;41:19–24. Japanese.

[34] Yashiro S, Ogi K, Yoshimura A, Sakaida Y. Characterization of high-velocity
impact damage in CFRP laminates: Part II – prediction by smoothed particle
hydrodynamics. Compos Part A. 2014;56:308–318.

[35] Geubelle PH, Baylor JS. Impact-induced delamination of composites: a 2D
simulation. Compos Part B. 1998;29(5):589–602.

[36] Toyama N, Ye J, Kokuyama W, Yashiro S. Non-contact ultrasonic inspection of
impact damage in composite laminates by visualization of Lamb wave
propagation. Appl Sci. 2019;9(1):46.

Appendix

Lamb wave propagation oblique to surface fiber orientation

In actual inspections, delamination may be evaluated based on Lamb wave propagation
oblique to the surface fiber orientation. When Lamb waves propagated obliquely to
(e.g., at $\theta = 45°$) the surface fiber orientation in the cross-ply laminate $[0_4/90_4]_S$, they
passed through the entire laminate and sublaminates comprised $[45_4/-45_4]_S$, $[45_4/-45_8]_T$,
and $[45_4]_T$. Therefore, the same dynamic finite element analysis as in Section 3.2 was
performed with the stacking sequence $[45_4/-45_4]_S$. Figure 14 shows the numerical
results of the Lamb wave propagation and maximum-amplitude map. The incident S0
mode was converted to the A0 one in the delaminated region (Fig. 14a and c), similar to
Figs. 9 and 11. However, the maximum-amplitude map generated for the S0 (and mode-
converted) waves (Fig. 14b and d) did not characterize the delamination outline,
because the amplitude of the incident S0 and converted A0 modes propagating at $\theta =$
45° was lower than that at $\theta = 0°$ and 90°. Moreover, the incident A0 mode was

repeatedly reflected in the delaminated region and standing waves of the A0 mode were generated on the back surface (Fig. 14e and f), whereas multiple reflections of the incident A0 mode were unobservable on the front surface (Fig. 14g and h). This was because the sublaminate $[45_4]_T$ exhibited much lower flexural stiffness than $[45_4/-45_8]_T$ and the same mechanisms as the sublaminates $[90_4/0_8]_T$ and $[90_4]_T$ were observed. The above results indicate that the fundamental insight of this study is applicable to oblique incident cases. The only exception is that the standing waves owing to multiple reflections of the S0/A0-mode-converted wave cannot be utilized.

Table titles and figure captions

Table 1. Material properties of CFRP (T700SC/2592) laminate [33,34].

Table 2. Sublaminate flexural stiffnesses calculated based on classical lamination theory.

Figure 1. C-scan images of specimen delamination: (a) film-inserted and (b) impact-induced cross-ply laminates.

Figure 2. Photographs of (a) fixed-point transducer and scanning laser and (b) *vice versa* (F/S and S/F systems, respectively), for ultrasonic excitation and reception.

Figure 3. Measurement condition schematic: (a) laser scanning area and fixed transducer position at $\theta = 0$ and 90° incident angles and (b) front and back surfaces inspected using laser scanning.

Figure 4. Dispersion curves of Lamb waves in possible stacking sequences of specimen and sublaminate for waves propagating at $\theta = 0$ and 90° incident angles.

Figure 5. Experimentally visualized Lamb waves propagating on back surface of film-inserted cross-ply laminate. All snapshots were plotted using red/green/blue (RGB) scale wherein negative and positive amplitudes were mapped from blue to red and green indicated midrange values (approximately 0).

Figure 6. Maximum-amplitude maps extracted from visualized waves propagating on back surface of film-inserted cross-ply laminate. All images were plotted using RGB scale wherein absolute amplitudes ranging from minimum to maximum were mapped from blue to red, respectively, and green indicated midrange values.

Figure 7. Experimentally visualized Lamb wave propagation on and corresponding maximum-amplitude map generated for front surface of film-inserted cross-ply laminate. All images were plotted in same manner as those plotted in Figs. 5 and 6.

Figure 8. Numerical model used to investigate mechanisms of Lamb wave propagation in delaminated laminate.

Figure 9. Numerical results of Lamb wave propagation (out-of-plane displacement) in

and maximum-amplitude map generated for delaminated cross-ply laminate. All images were plotted in same manner as those plotted in Figs. 5 and 6.

Figure 10. Numerical results of Lamb wave propagation (out-of-plane displacement) in cross-section of delaminated cross-ply laminate when incident A0 mode reached delaminated region. All images were plotted in same manner as those plotted in Fig. 5, and dimension in through-thickness direction was five times larger than that in in-plane direction.

Figure 11. Numerical results of Lamb wave propagation (out-of-plane displacement) in cross-section of delaminated cross-ply laminate when only incident S0 mode reached delaminated region. All images were plotted in same manner as those plotted in Fig. 5, and dimension in through-thickness direction was five times larger than that in in-plane direction.

Figure 12. Experimentally visualized Lamb wave propagation on and corresponding maximum-amplitude map generated for back surface of cross-ply laminate exhibiting barely visible impact damage (BVID).

Figure 13. Experimentally visualized Lamb wave propagation on and corresponding maximum-amplitude map generated for front surface of cross-ply laminate exhibiting barely visible impact damage (BVID).

Figure 14. Numerical results of Lamb wave propagation (out-of-plane displacement) and maximum-amplitude map when Lamb waves propagated at $\theta = 45°$ in delaminated cross-ply laminate. All images were plotted in same manner as those plotted in Figs. 5 and 6.

Tables

Table 1. Material properties of CFRP (T700SC/2592) laminate [33,34].

Longitudinal Young's modulus [GPa]	132
Transverse Young's modulus [GPa]	9.85
In-plane shear modulus [GPa]	5.25
Out-of-plane shear modulus [GPa]	3.80
In-plane Poisson's ratio [-]	0.25
Out-of-plane Poisson's ratio [-]	0.38
Density [g cm^{-3}]	1.80

Table 2. Sublaminate flexural stiffnesses calculated based on classical lamination theory.

Stacking sequence	Flexural stiffness D_{11} [GPa·mm^3]
$[0_4]_T$	1.38
$[90_4]_T$	0.103
$[0_4/90_8]_T$	19.4
$[90_4/0_8]_T$	20.7

Figures

(a) Specimen I   (b) Specimen II

Figure 1. C-scan images of specimen delamination: (a) film-inserted and (b) impact-induced cross-ply laminates.

Figure 2. Photographs of (a) fixed-point transducer and scanning laser and (b) *vice versa* (F/S and S/F systems, respectively), for ultrasonic excitation and reception.

Figure 3. Measurement condition schematic: (a) laser scanning area and fixed transducer position at $\theta = 0$ and 90° incident angles and (b) front and back surfaces inspected using laser scanning.

Figure 4. Dispersion curves of Lamb waves in possible stacking sequences of specimen and sublaminate for waves propagating at $\theta = 0$ and 90° incident angles.

Figure 5. Experimentally visualized Lamb waves propagating on back surface of film-inserted cross-ply laminate. All snapshots were plotted using red/green/blue (RGB) scale wherein negative and positive amplitudes were mapped from blue to red and green indicated midrange values (approximately 0).

Figure 6. Maximum-amplitude maps extracted from visualized waves propagating on back surface of film-inserted cross-ply laminate. All images were plotted using RGB scale wherein absolute amplitudes ranging from minimum to maximum were mapped from blue to red, respectively, and green indicated midrange values.

S/F system + Front surface + $\theta = 0°$		S/F system + Front surface + $\theta = 90°$	
Wave propagation	Max. amp. map	Wave propagation	Max. amp. map
(a) 20 μs	(b) 0–20 μs	(c) 20 μs	(d) 0–20 μs
(e) 40 μs	(f) 0–100 μs	(g) 40 μs	(h) 0–100 μs

Figure 7. Experimentally visualized Lamb wave propagation on and corresponding maximum-amplitude map generated for front surface of film-inserted cross-ply laminate. All images were plotted in same manner as those plotted in Figs. 5 and 6.

Figure 8. Numerical model used to investigate mechanisms of Lamb wave propagation in delaminated laminate.

Figure 9. Numerical results of Lamb wave propagation (out-of-plane displacement) in and maximum-amplitude map generated for delaminated cross-ply laminate. All images were plotted in same manner as those plotted in Figs. 5 and 6.
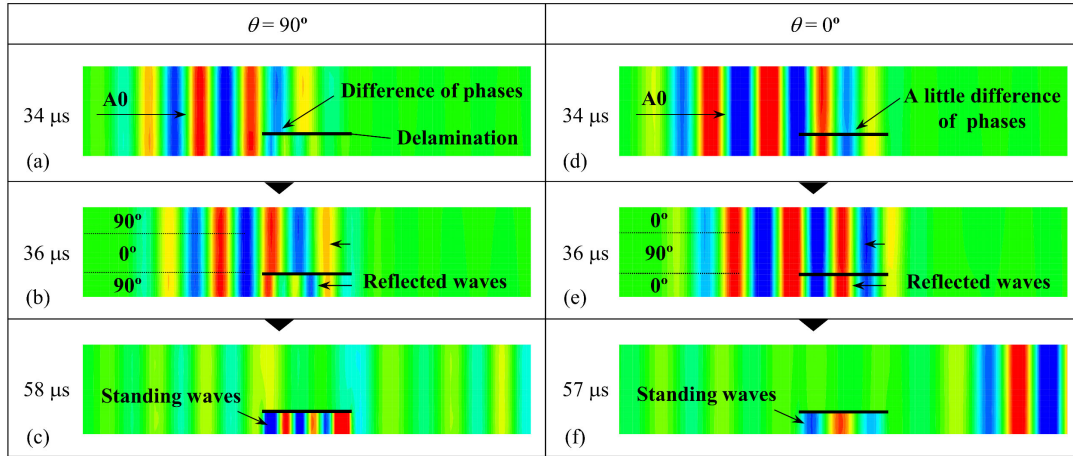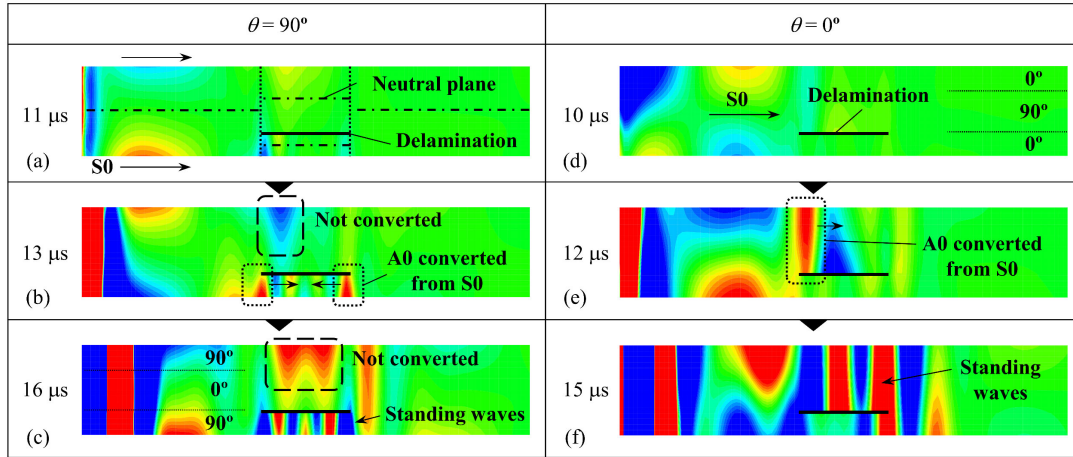

Figure 10. Numerical results of Lamb wave propagation (out-of-plane displacement) in cross-section of delaminated cross-ply laminate when incident A0 mode reached delaminated region. All images were plotted in same manner as those plotted in Fig. 5, and dimension in through-thickness direction was five times larger than that in in-plane direction.
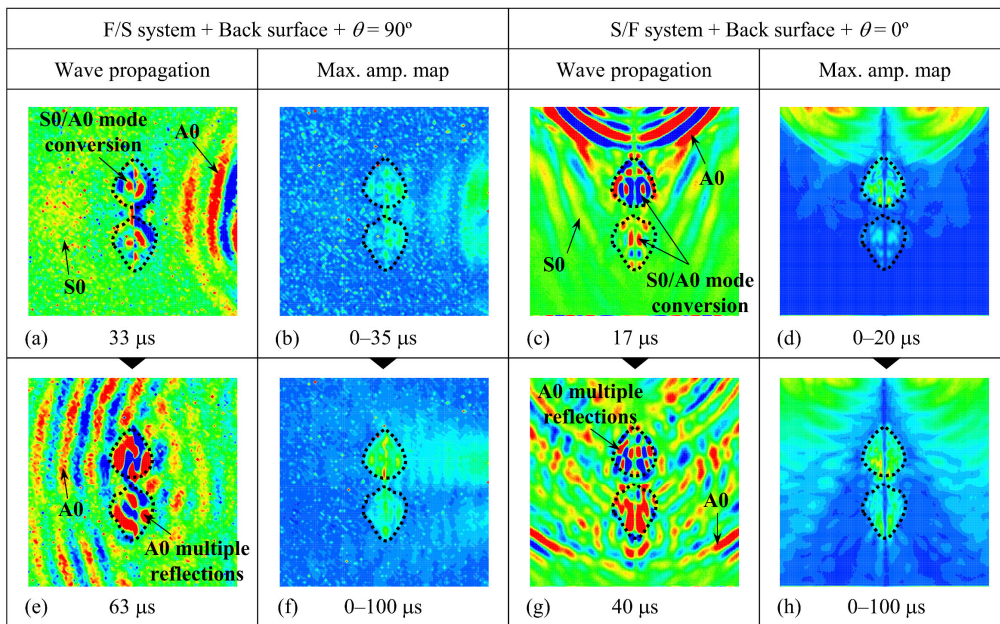
Figure 11. Numerical results of Lamb wave propagation (out-of-plane displacement) in cross-section of delaminated cross-ply laminate when only incident S0 mode reached delaminated region. All images were plotted in same manner as those plotted in Fig. 5, and dimension in through-thickness direction was five times larger than that in in-plane direction.

Figure 12. Experimentally visualized Lamb wave propagation on and corresponding maximum-amplitude map generated for back surface of cross-ply laminate exhibiting barely visible impact damage (BVID).
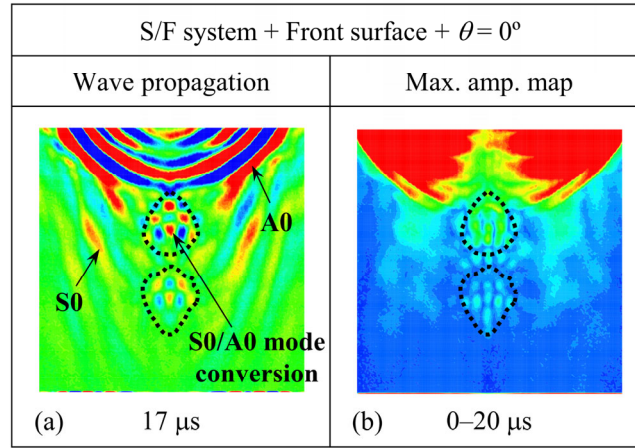
Figure 13. Experimentally visualized Lamb wave propagation on and corresponding maximum-amplitude map generated for front surface of cross-ply laminate exhibiting barely visible impact damage (BVID).
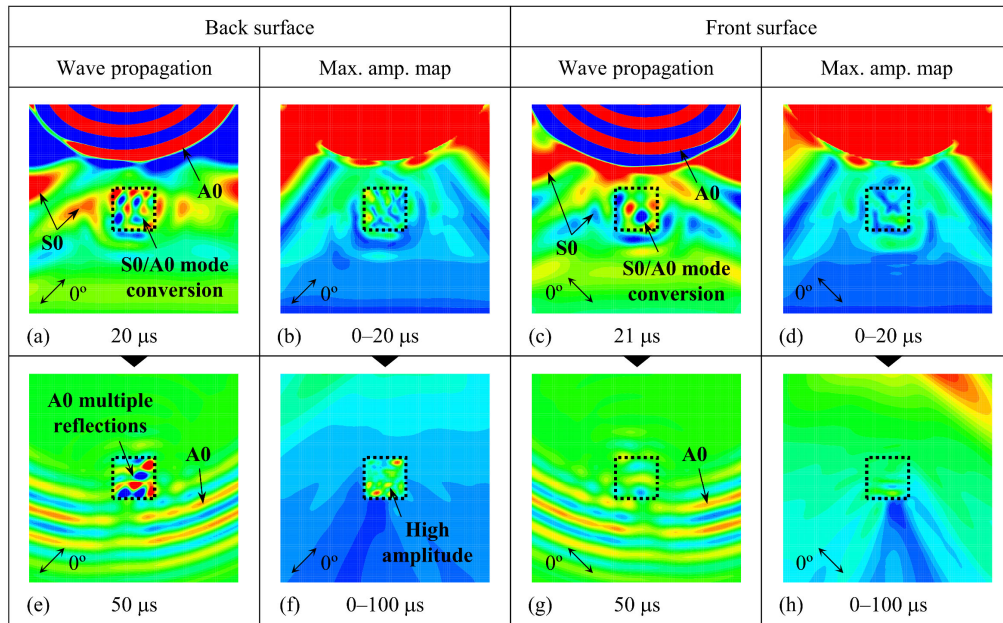

Figure 14. Numerical results of Lamb wave propagation (out-of-plane displacement) and maximum-amplitude map when Lamb waves propagated at $\theta = 45°$ in delaminated cross-ply laminate. All images were plotted in same manner as those plotted in Figs. 5 and 6.